THE ASTROPHYSICAL JOURNAL, 383:269–279, 1991 December 10

SPECTRAL SIGNATURES OF THE MeV–PeV RADIATION FROM ACCRETING NEUTRON STARS

B. RUDAK[1] AND P. MÉSZÁROS[2]
525 Davey Laboratory, Pennsylvania State University, University Park, PA 16802
Received 1991 April 25; accepted 1991 June 17

ABSTRACT

We discuss the formation of the high-energy gamma-ray and neutrino spectrum produced by the injection of a power-law proton distribution extending up to $E_p \sim 10^{16}$ eV in the magnetosphere of accreting neutron stars. The resulting proton spectrum is calculated in the presence of advection and cooling by interactions with the X-ray spectrum of the neutron star, leading to several components of a secondary photon spectrum extending from the MeV to the PeV range, and a neutrino spectrum extending from about 0.1 TeV to 0.1 PeV. The shapes of the resulting high-energy secondary spectra depend sensitively on the accreting source's X-ray spectrum and energy density as well as the magnetic field strength involved. Detailed spectra are calculated for the specific examples of Her X-1 and Cyg X-3.

Subject headings: gamma rays: bursts — neutrinos — radiation mechanisms — stars: accretion — stars: neutron — X-rays: binaries

1. INTRODUCTION

A number of accreting X-ray pulsars (AXPs) have been reported as sporadic very high energy (VHE) or ultrahigh-energy (UHE) sources, corresponding to the TeV or PeV range. The latest status of such observations is reviewed, e.g., in Fegan (1990). Among objects where positive detections were reported at either VHE or UHE by more than one group are such well-known AXPs as Her X-1, Vela X-1, 4U 0115+63, and LMC X-4. These sources appear to have time signatures at these energies which correspond closely to the previously known X-ray pulse and/or orbital periods. Another well-known X-ray source reported many times at these energies is Cyg X-3, which at VHE/UHE energies reportedly shows a 4.8 hr orbital period as it does in X-rays (e.g., Bonnet-Bidaud and Chardin 1988). While there is no direct X-ray evidence to prove that this is an accreting X-ray pulsar, its X-ray continuum is hard and not unlike that of an AXP, so we shall assume here tentatively that it belongs in this class together with the previous sources. There is much uncertainty concerning the degree of confidence to be ascribed to the VHE/UHE observations, owing to questions of techniques, statistics, and repeatability (e.g., Weekes 1988, 1990; Fegan 1990). For this reason, it appears useful to explore on theoretical grounds what kind of spectral signatures might be present in these objects in the TeV–PeV range, and also at lower MeV–GeV energies where the photon number is larger and where measurements can be made using well-tested techniques with instruments such as those on the *GRO* spacecraft.

In this paper we present calculations of the gamma-ray spectrum in the MeV–PeV range which are valid in a variety of situations involving shock acceleration or any other mechanism injecting protons with a power-law energy distribution into a region containing a magnetic field $B \sim 10^5$–10^7 G and a background of preexisting X-ray photons. The energetic protons, interacting with a source-specific magnetic field and X-ray photons, produce a characteristic gamma-ray spectrum which can be compared with observations, and may provide useful constraints on models as well as a benchmark against which to analyze existing or planned observations. In § 2 we give a description of a specific case, the corotating jet model of Király & Mészáros (1988), which is used as an example for working out quantitative numerical details. In § 3 we discuss the constraints imposed on the proton energy distribution by the presence of the magnetic field, the specific radiation field, and the character of the accretion flow, and we determine the region of dominance in the γ_p-B parameter space of the different processes involving protons, in particular $p\gamma$ processes. In § 4 we discuss the properties of the proton-photon interactions. These interactions are utilized in § 5 to calculate the high-energy photon and neutrino spectra expected to be formed in the two prototypical sources Her X-1 and Cyg X-3. In § 6 we present our conclusions as well as a discussion of prospects of observational comparisons with anticipated *GRO* and DUMAND results.

2. A SPECIFIC MODEL

As mentioned above, our results are essentially model-independent. However, in order to visualize the physical situation, it appears useful to carry out the calculations within the framework of a specific model. An observational fact characterizing the identified VHE/UHE accreting pulsars is that their spin rate is near the corotation rate: the Kepler velocity of the accretion disk at the magnetospheric (Alfvén) radius is close to the rotation speed of the magnetosphere itself. This was used by Király & Mészáros (1988, herafter KM) as the basis for a corotating jet model, in which some of the accreting matter is assumed to be occasionally ejected by the radiation pressure along the magnetic axis out of the Alfvén surface, where it is shocked (see Fig. 2 of KM). Since the matter is ejected from near the stellar surface, this can tap a substantial fraction of the gravitational potential energy achieved by the accreted matter in falling in, which can result in instantaneous luminosities approaching the Eddington value. Since the X-ray spin period of sources near corotation is generally not stable, with $\dot{P}$ alternating quasi-randomly between spin-up and spin-down, one

[1] On leave from N. Copernicus Astronomical Center, Toruń, Poland.
[2] On leave at Harvard-Smithsonian Center for Astrophysics during part of this work.

expects that the strict corotation condition is only occasionally achieved, leading to sporadic ejection events accompanied by the appearance of VHE/UHE emission.

When the corotation condition is approximately satisfied, protons reaching the Alfvén surface can be scattered up and down across the shock enough times to get up to PeV energies, without suffering significant advection sideways which would carry them out of the acceleration region. A large fraction of the protons produce TeV–PeV gamma rays by photopion and other processes, which are not degraded by magnetic one-photon pair production, since the field at the Alfvén radius is weak enough so that those photons which are propagating close to the magnetic axis are below threshold. Because of the rotation and collimation by magnetic absorption of the off-axis gamma rays, the escaping gamma rays are expected to be beamed, leading to pulsations. Some protons which are not converted to gamma rays at the Alfvén surface may escape the accleration region and continue to propagate beyond this region, which could lead to additional gamma rays when they interact with a column depth of gas of ~ 50–200 g cm^{-2}, provided either by a warp in the accretion disk or by the edge of the companion star's atmosphere (see Fig. 3 of KM). The periodic coverage by the accretion disk may provide the long-term X-ray modulation effects, e.g., the 35 day ON-OFF X-ray behavior in Her X-1. Gamma rays would therefore be expected just before egress and after ingress into eclipse of the X-rays by the star (modulation at the orbital period) or by the disk (35 day period in Her X-1). However, Her X-1 is a rare example in the richness of its temporal behavior. So far, most other VHE/UHE sources in which periodicities have been reported appear to exhibit only spin and/or orbital modulations, and the statistics are less significant than for the DC detection. For this reason, in this paper we do not address questions relating to periodicities. In what follows we concentrate on the main mechanisms of VHE/UHE radiation produced in the acceleration region near the neutron star by interaction with the X-ray radiation field.

3. PROTON ACCELERATION

We assume a shock acceleration mechanism of the diffusive type, and consider a proton source function of a power-law type,

$$Q_p \propto E_p^{-\Gamma_p}, \tag{1}$$

where $\Gamma_p \simeq 2$ is expected for strong shocks where the compression ratio is 4 (Axford 1981). The distribution of proton energies $N_p(E_p)$ at the shock site depends on (1) the efficiency of the advection process (i.e., removal of protons from the region above the shock) and (2) the proton cooling processes. Our aim is to determine self-consistently the resulting proton energy distribution, and to use this to calculate the spectra of the secondary particles (photons and neutrinos).

In considering the total energetics of the secondary particles generated, the advection of protons out of the acceleration region is of prime importance. In the particular case of the corotating jet model, we expect the shock to form at the Alfvén shell located at r_A (see KM). Since the character of the accretion flow in the vicinity of the Alfvén shell is not known with certainty, we shall consider two extreme cases: radial infall and disk accretion. Insofar as the ultrarelativistic protons are magnetically coupled to the accreting matter, the rate of proton cooling will be reduced if the typical time t_{adv} that protons spend within the acceleration/cooling region is shorter than the characteristic cooling time. Therefore, we expect the relative fraction of the total proton luminosity converted into photon and neutrino luminosity to be a strong function of the accretion character (radial infall versus disk accretion). For the observed TeV–PeV accreting pulsars the magnetospheric radius r_A happens to fall close to r_{cor}, the corotation radius. In the case of disk accretion, no transverse advection occurs if $r_A = r_{cor}$, since both the magnetosphere and the disk rotate together at the Kepler velocity. If, however, $r_A = \delta r_{cor}$, with δ near but not exactly unity (see KM), then the advection velocity V_{adv} may attain values of the order of $0.01c$. In the case of spherical accretion, V_{adv} becomes of the order of $0.1c$, and may eventually play a major role in regulating the maximal value of the proton energy.

The main proton cooling processes in the neighborhood of a magentized accreting neutron star are expected to be (*a*) proton synchrotron radiation ($p\boldsymbol{B}$), (*b*) proton-photon interactions ($p\gamma$) resulting in photomesons or $e^{\pm}$-pairs, denoted as ($p\gamma$, π) and ($p\gamma$, $e^{\pm}$), respectively, and (*c*) proton-proton interactions (pp). In the calculations that follow we have not included the effect of the (pp) reactions, which would occur, if at all, mainly well beyond the magnetosphere. This simplification does not affect significantly the shape of the distribution $N_p(E_p)$ in the high-energy range, i.e., $E_p \geq 10^4$ GeV, since here the ($p\gamma$) and ($p\boldsymbol{B}$) processes dominate, unless the density of the accreting plasma is unusually high (at least 10^{14} cm^{-3}).

The proton cooling mechanisms are mainly responsible for introducing any departures of the distribution $N_p(E_p)$ from the functional form given in equation (1). They also impose the most significant constraints on the maximum attainable proton energy, $E_{p,max}$, or, equivalently, the maximum proton Lorentz factor, $\gamma_{p,max}$. This is given by

$$\gamma_{p,max} = \min(\gamma_{p,eq}; \gamma_{p,conf}), \tag{2}$$

where $\gamma_{p,eq}$ is a steady state equilibrium value for the proton energy balance between heating and cooling, while $\gamma_{p,conf}$ comes from the requirement of proton confinement, which may be expressed by demanding that the mean free path for proton scattering, λ_{mfp}, should not exceed the characteristic size of the region ($\sim 10^8$ cm for the Alfvén radius).

Unlike the more frequently considered proton beam-dump models [involving (pp) interactions, with the total cooling dominated by the ($p\boldsymbol{B}$) synchrotron process], for the circumstances of this model the more important mechanism is the ($p\gamma$) cooling mechanism. The density of X-ray and/or ultraviolet radiation typical for the sources mentioned in § 1 is in fact high enough for ($p\gamma$) interactions to compete effectively with ($p\boldsymbol{B}$). In Figure 1 we show the value of $\gamma_{p,max}$ as a function of the magnetic field strength B in the presence of a standard diffusive shock acceleration in a radiation field with $L_X = 3 \times 10^{37}$ ergs s^{-1}. This is obtained using the acceleration rates of Axford (1981) and the cooling rates of equations (3a) and (3b) and assuming a scattering length $\lambda_{mfp} = 10 r_g$, where r_g is the proton gyroradius. Also shown in Figure 1 are the regions where either ($p\boldsymbol{B}$) or ($p\gamma$) dominates the proton cooling.

4. BASIC INTERACTIONS

Once the protons have been accelerated to ultrarelativistic energies, they can produce TeV–PeV photons via ($p\gamma$) and (pp) interactions. For the AXP model we are considering here, it is the former type of interaction that is dominant (see also, e.g., Mitra 1990). For this reason it is convenient to neglect the (pp) interactions, which introduces a twofold simplification: (1) one

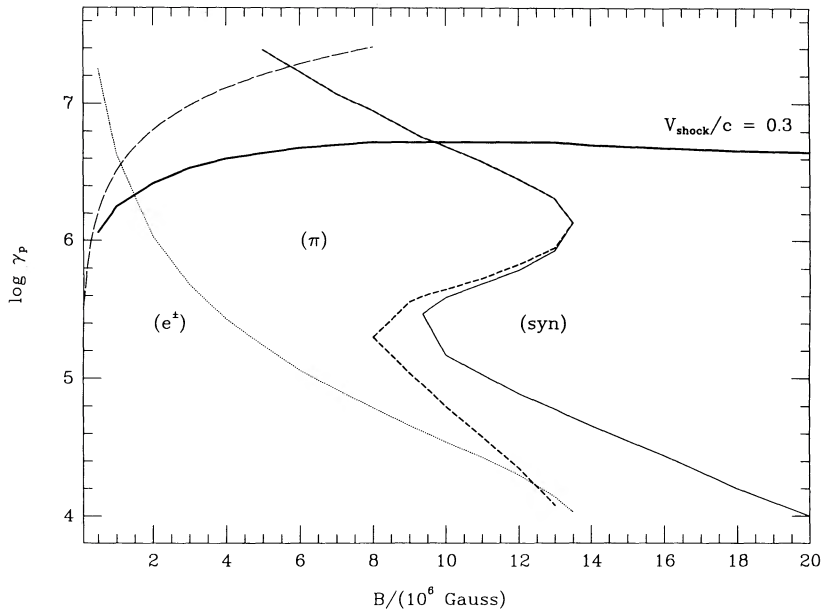

FIG. 1*a*

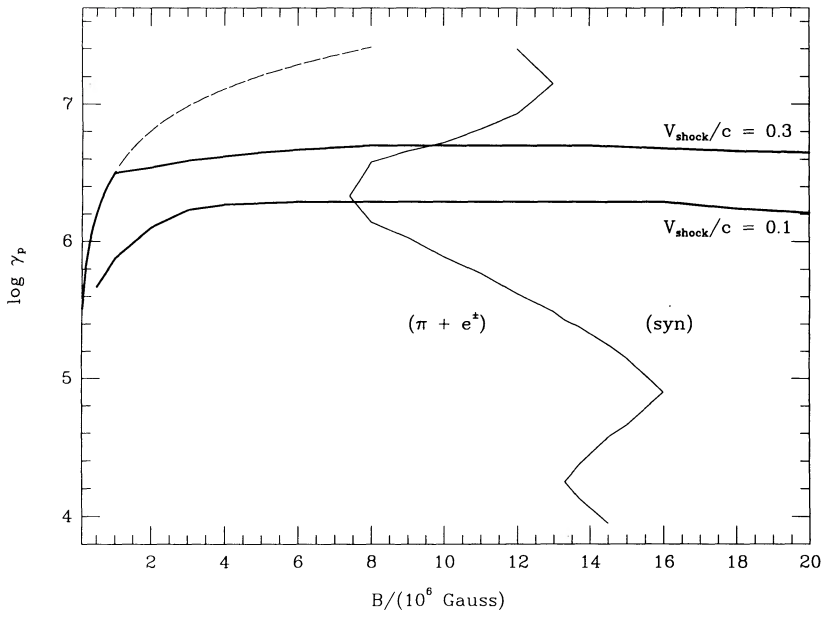

FIG. 1*b*

FIG. 1.—(*a*) Maximum possible Lorentz factor (*thick lines*) attained by protons via the diffusive shock acceleration, shown as a function of the magnetic field. The mean free path for proton scattering was assumed to be 10 times the Larmor radius. The confinement limit $\gamma_{p,\,conf}$ is sketched with the long-dashed line. The cooling of protons proceeds via the ($p\boldsymbol{B}$) and ($p\gamma$) processes. The thin continuous line separates the regions of dominance of the two cooling processes. Within the region of ($p\gamma$) dominance, the contribution from photopion production (*short-dashed line*) and pair creation (*dotted line*) is shown separately. In this example, the energy density of the X-ray photons is 10^{10} ergs cm^{-3}, shared equally by a blackbody component with $T_{bb} = 6 \times 10^5$ K and a power-law component stretching from 0.1 to 50 keV with energy spectral index $\alpha = 0.5$. (*b*) Similar to (*a*), but the soft X-ray blackbody component has been replaced by an extreme UV blackbody component with $T_{bb} = 6 \times 10^4$ K. Two solutions for $\gamma_{p,\,max}$ are shown for two values of the shock velocity.

need not be concerned about the presence of an appropriate material target of finely tuned grammage in order to produce gamma rays, and (2) the maximal photon energy achievable in the photopion decay can be almost one order of magnitude higher than in the case of (pp). This is because, for a Lorentz factor of 10^4 or higher, protons involved in (pp) reactions yield pions with substantial multiplicities (Orth & Buffington 1976), which can be as high as $\sim$20 (e.g., Lang 1980), whereas the multiplicity of pions produced in ($p\gamma$) on the X-ray photons in the AXPs can hardly exceed a value of unity, even for $\gamma_p \sim 10^7$.

In this simplified situation, the ultrahigh-energy photons and neutrinos are produced via ($p\gamma$, π) reactions: neutral pions decay directly into TeV–PeV photons ($\pi^0 \rightarrow 2\gamma$), while charged pions eventually yield electron/positron pairs and neutrinos ($\pi^{\pm} \rightarrow \mu^{\pm} + \nu_{\mu}(\tilde{\nu}_{\mu}) \rightarrow e^{\pm} + \tilde{\nu}_{\mu} + \nu_{\mu} + \nu_e(\tilde{\nu}_e)$. These $e^{\pm}$ pairs are energetic enough to radiate TeV or even PeV photons by syn-

chrotron ($e^{\pm}\boldsymbol{B}$) in the presence of the AXP field near the magnetospheric boundary. However, the magnitude of the ($e^{\pm}\boldsymbol{B}$) contribution is controlled by two earlier synchrotron contributions, the ($\pi^{\pm}\boldsymbol{B}$) and ($\mu^{\pm}\boldsymbol{B}$). The mean lifetime of charged pions (2.6×10^{-8} s) and muons (2.2×10^{-6} s) is long enough that for the high Lorentz factors which these particles acquire most of their energy will be lost in the form of synchrotron photons with energies definitely not falling within the TeV–PeV range. As a result, the VHE/UHE spectrum will be accompanied by an additional, more easily measurable gamma-ray component below several tens of GeV, formed via ($\pi^{\pm}\boldsymbol{B}$), ($\mu^{\pm}\boldsymbol{B}$), ($p\boldsymbol{B}$), and ($p\gamma$, $e^{\pm}$) followed by ($e^{\pm}\boldsymbol{B}$) synchrotron.

The efficiency of the various processes can be parameterized by the means of the corresponding particle cooling rates, identified by the reciprocals of the e-folding time scale for the particle energy decrease, i.e., $\Lambda(\mathrm{proc}) \equiv -(\dot{\gamma}_x)_{\mathrm{proc}}/\gamma_x$. Therefore, for a particle x of mass m_x and Lorentz factor γ_x, the process ($x\boldsymbol{B}$) yields a cooling rate

$$\Lambda(x\boldsymbol{B}) = \frac{4}{3}\left(\frac{m_e}{m_x}\right)^3 \frac{c\sigma_{\mathrm{T}} u_B}{m_e c^2}\gamma_x , \tag{3a}$$

where u_B is the magnetic field energy density, and similarly the (pu, π) and ($p\gamma$, $e^{\pm}$) processes yield

$$\Lambda(p\gamma, i) = \frac{2\pi c}{\gamma_p^2}\int_{\tilde{x}}^{2\gamma_p x_{\max}} \sigma_i(x')K_i(x')x'\left[\int_{x'/2\gamma_p}^{x_{\max}} n(x)\,dx\right]dx' , \tag{3b}$$

where (i) indicates either photopions or $e^{\pm}$ pairs, σ_i and K_i are cross sections and inelasticity, respectively, $n(x)$ is the photon occupation number, x is the energy in $m_e c^2$ units, and $\tilde{x} \equiv \max[x_{\mathrm{th}}(i), 2\gamma_p x_{\min}]$. The threshold energy x_{th} equals 2 and 284 for creation of $e^{\pm}$ and pions, respectively (for head-on collisions). For the cross sections and inelasticity parameters, we used the experimental data and analytical fits described in Begelman, Rudak, & Sikora (1990, hereafter BRS).

Unlike the case of the proton acceleration rate and the synchrotron cooling rate, which have a simple energy dependence ($\propto \gamma_p^{-1}$ and $\propto \gamma_p$, respectively), the cooling rates given by equation (3b) can be rather complex. The typical X-ray photon spectra involved in the interactions consist generally of two components, which approximate a blackbody contribution and a power-law contribution, respectively, extending to the UV on one side and cutting off at hard X-ray energies on the other. The effect of such a composite X-ray spectrum is illustrated in Figure 1 by the S-shape of the curve delimiting the regions of the ($p\gamma$) and (p, $\boldsymbol{B}$) dominance.

In order to get some feel for the behavior of the cooling rates, we focus first on the most interesting range of γ_p values, $[10^4, 10^7]$, and consider for simplicity a pure power-law X-ray spectrum between 0.1 and 50 keV of energy spectral index α. This, combined with the fact that the threshold energies for ($p\gamma$, π) and ($p\gamma$, $e^{\pm}$) are different leads to different behaviors of the cooling rates as functions of γ_p. For $\gamma_p < 10^6$ we have $\Lambda(p\gamma, \pi) \propto \gamma_p^{\alpha}$, while for higher γ_p values it remains practically constant. At the same time, $\Lambda(p\gamma, e^{\pm})$ reaches its maximum at $\gamma_p \approx 3 \times 10^4$ and then drops roughly as $\gamma_p^{-0.5}$. The rate $\Lambda(p\gamma, \pi)$ dominates over $\Lambda(p\gamma, e^{\pm})$ everywhere. This trend is reversed only for very steep spectra for a narrow range of γ_p values (e.g., $\alpha = 1.5$ gives $\Lambda(p\gamma, \pi) < \Lambda(p\gamma, e^{\pm})$ for $\gamma_p \leq 5 \times 10^4$).

Introducing a blackbody component in addition to the power law can, however, change the previous relations substantially, provided that the energy density it carries (u_{bb}) is nonnegligible with respect to the energy density of the power-law component, u_{pl} (this is the case in Cyg X-3). As an example, suppose that $u_{\mathrm{pl}} = u_{\mathrm{bb}}$. If the blackbody photons are soft enough, they can keep $\Lambda(p\gamma, e^{\pm})$ constant throughout the entire range of γ_p (e.g., for $kT_{\mathrm{bb}} \simeq 0.1$ keV) or even cause it to jump up at $\gamma_p \sim x_{\mathrm{th}}(e^{\pm})m_e c^2/2kT_{\mathrm{bb}}$ by more than one order of magnitude before reaching a plateau (e.g., for $kT_{\mathrm{bb}} \simeq 5$ eV). Similarly, strong jumps occur for $\Lambda(p\gamma, \pi)$ at appropriate proton energies ($\gamma_p \sim x_{\mathrm{th}}(\pi)m_e c^2/2kT_{\mathrm{bb}}$). Generally speaking, introducing a blackbody component increases radically the likelihood of $e^{\pm}$ creation. This is particularly true when the power-law component is rather flat ($\alpha < 1$) and the blackbody peaks at UV energies. Then the dominance of photopair over photopion production extends almost over two decades in γ_p, and is located in the middle of the $[10^4, 10^7]$ range. These relations between the rates determine ultimately the shape of the electromagnetic spectrum at higher energies. For example, a strong blackbody component in the ultraviolet would result in a prominent feature at ~ 1 MeV energies and a relatively smaller PeV component.

Besides the cooling rates of equations (3), there is another quantity which enters explicitly into the expressions for the final electromagnetic spectra, and that is the effective inelasticity K_i^{eff}, where the index i stands for either π or $e^{\pm}$. This is the ratio of the energy loss rate to the interaction rate, obtained using equation (3b) as

$$K_i^{\mathrm{eff}} = \Lambda(p\gamma, i)\left[\frac{2\pi c}{\gamma_p^2}\int_{\tilde{x}}^{2\gamma_p x_{\max}} \sigma_i(x')x'\left[\int_{x'/2\gamma_p}^{x_{\max}} n(x)\,dx\right]dx'\right]^{-1} . \tag{4}$$

The effective inelasticity is generally a function of γ_p for any given X-ray spectrum. In the simplest case of the power-law spectrum mentioned above, K_π^{eff} starts off at 0.14 for the minimal allowed $\gamma_p (\sim 1.4 \times 10^3$ in this example), then increases by a factor of 2 over the next three decades of γ_p, and reaches 0.5 at $\gamma_p \approx 10^7$. In practice, the details of the functional dependence K_π^{eff} versus γ_p do not matter a lot as long as K_π^{eff} is confined to such a narrow range of values. This is not the case, however, with K_e^{eff}. It stays roughly constant ($\sim 5 \times 10^{-4}$) for low values of γ_p, but between $\gamma_p \approx 10^4$ and $\gamma_p \approx 10^7$ it drops by two orders of magnitude. That has an immediate impact on the shape and the location of the ($p\gamma$, $e^{\pm}$) component in the photon energy spectrum. The typical energy of a photon produced by a proton with Lorentz factor γ_p in a ($p\gamma$, $e^{\pm}$) reaction is proportional to $B_m(K_e^{\mathrm{eff}}\gamma_p)^2$, i.e., it does not depend strongly on γ_p for $\gamma_p > 10^4$ ($\propto B_m g_p^{0.6}$).

5. HIGH-ENERGY PHOTON AND NEUTRINO SPECTRA

We calculate now as two prototypical examples the high-energy photon and neutrino spectra expected from Her X-1 and Cyg X-3 in the high state (or objects with similar X-ray spectra and magnetic fields as assumed). We utilize a simplified spectral calculation similar to that used in BRS for the case of AGNs. Details of the cross sections and of the spectral calculation procedure are to be found in that reference. The main difference with our present case is that, because of the more involved X-ray spectral input and the different environment, a largely numerical treatment is required. The cases of Her X-1 and Cyg X-3 were chosen because they are two of the most studied sources, which exhibit substantial differences in their X-ray spectra and luminosities as well as different VHE/UHE characteristics.

The time-averaged Her X-1 spectrum contains a soft X-ray component which may be fitted by a blackbody spectrum with $kT_{bb} = 0.11$ keV, and a hard X-ray component resembling a power-law spectrum with an energy spectral index $\alpha \approx 0.5$ and an abrupt break at $E_{break} \approx 20$ keV (McCray *et al.* 1982). The luminosity in the hard X-ray component is almost one order of magnitude higher than the total luminosity of the soft X-ray part, while the overall luminosity in X-rays is $L_X = 2.8 \times 10^{37}$ ergs s^{-1}. This has to be translated for our purposes into an X-ray energy density u_X, which enters equation (3b) via $n(x)$. At a putative shock distance $R = r_A \sim 10^8$ cm this is $u_X = 7.4 \times 10^9(1 + \tau_{es}/3)R_8^{-2}$ ergs cm^{-3}. We allowed here for a possible decrease in the photon diffusion velocity due to electron scattering over a region of a physical size $R_8 \times 10^8$ cm. The optical depth of the AXP magnetosphere against electron scattering may possibly reach unity, so that we took $u_X = 10^{10} R_8^{-2}$ ergs cm^{-3} for Her X-1.

The spectrum of Cyg X-3 changes drastically (especially below 10 keV) when the object switches from the high- to the low-intensity state. As an example we chose to consider the case of the high state, with $L_X = 2 \times 10^{38}$ ergs s^{-1} (Bonnet-Bidaut & Chardin 1988). In this high state, the most prominent spectral feature can be approximated by a blackbody with $kT_{bb} = 1.2$ keV. In addition to this, there is also a power-law component with an energy spectral index $\alpha \approx 1$ extending at least up to ~ 50 keV (White & Holt 1982). The blackbody component, being much harder than in case of Her X-1, provides about 68% of the total L_X. In our calculations we used $u_X = 6 \times 10^{10} R_8^{-2}$ ergs cm^{-3} for Cyg X-3.

Several other parameters entering the calculations are subject to some uncertainty. One of these is the value of the magnetic field in the acceleration region. It is difficult to calculate an exact value of B_m at the magnetosphere even in the case of Her X-1, which has a well-determined field at the surface of the neutron star ($B_* \sim 3.5 \times 10^{12}$ G; e.g., KM or Mihara et al. 1990). This is because so far one does not know exactly either the location of the magnetosphere or the real dependence of B on radius (in addition to a dipole-like character, one may expect some extra components, especially in the magnetospheric region). This is a sensitive parameter, since the flux level contributed by proton synchrotron radiation scales roughly as B_m^2, and therefore even a factor of 5 uncertainty in the value of B_m would produce different-looking spectra below 1 GeV. The uncertainty in B_m affects also the appearance of the spectrum in the very high energy range (see results below). For the purposes of this calculation we took illustrative magnetospheric values of $B_m = 5 \times 10^6$ G for Her X-1, while for the Cyg X-3 we considered B_m in the range 10^5 to 5×10^7 G. Both limits in this range are completely arbitrary, since there is so far no direct observational evidence for a magnetic field in Cyg X-3, such as the cyclotron line seen in Her X-1. However, for B_m below 10^5 G, $\gamma_{p,\,conf}$ becomes uninterestingly low, while the upper limit of B_m comes from the corotation condition for $P_{rot} = 13$ ms. As an arbitrary "canonical" magnetospheric field B_m for Cyg X-3 we take 10^6 G, and the more detailed spectra for this source which are separated into the components are provided for this specific value. Another free parameter entering the calculation is the ratio of the scattering mean free path to the gyroradius, λ_{mfp}/r_g, which appears in the acceleration rate. For strong shocks this is expected to be between 1 and 10 (Kazanas & Ellison 1986) or higher. We took this ratio to be 10 for Her X-1 and 5 for Cyg X-3.

With the physical conditions as described above, we are now able to solve the steady state kinetic equation for the proton distribution function $N_p(E_p)$ in the presence of a source term, cooling mechanisms, and advection:

$$\frac{\partial}{\partial E_p}\left[N_p E_p \Lambda(\mathrm{tot})\right] = N_p/t_{adv} - Q_p \,. \tag{5}$$

The functional dependence of $N_p(E_p)$ deviates from the original E_p^{-2} at those proton energies where the total proton cooling rate $[\Lambda(\mathrm{tot}) = \Lambda(p\boldsymbol{B}) + \sum_i \Lambda(p\gamma, i)]$ exceeds the advection rate (t_{adv}^{-1}). Therefore, while in the low-energy range the E_p^{-2} dependence remains intact, the high-energy part is already steepening at $\gamma_p \sim 10^4$. The changes appearing in the initial proton distribution are most easily visible when considering the energy spectrum of the "surviving" protons which escape or are carried away by advection (downstream side of the shock). Their luminosity per logarithmic bandwidth,

$$dL_p(\mathrm{adv})/\mathrm{d}\ln E_p \propto Q_{adv} E_p^2 \,, \tag{6}$$

where $Q_{adv} \equiv N_p/t_{adv}$, is shown in Figure 2. This is normalized to the total luminosity initially injected into relativistic protons,

$$L_p(\mathrm{inj}) \propto \int_{m_p c^2}^{E_{p,\max}} Q_p(E_p) E_p \, d E_p \,,$$

which is kept as a free parameter throughout the paper. The complementary portion of the proton energy spectrum which neither escapes nor gets advected (i.e., the difference between the dot-dash injected spectrum idealized as a step function and the full-line actual proton spectra of Fig. 2) represents the fraction of the injected energy that is converted into secondary radiation in the form of photons and neutrinos. The fraction of the proton energy going into secondary radiation via the $(p\gamma)$ and $(p\boldsymbol{B})$ reactions is substantial for low values of the advection velocity (more than 10% for $V_{adv} = 0.01c$). A substantial fraction of the advected protons is likely to be subsequently recycled by the accretion stream and redirected toward the acceleration region. In the KM model, a fraction of the protons may also escape the magnetosphere, and if the magnetic channeling is favorable, they may interact further with material in the accretion flow or the binary stellar companion, in which case the expected contribution to the spectrum below the TeV range would need to be modified to take these effects into account in the N_p distribution. Another fraction of advected protons could also conceivably interact with the neutron star itself, leading mainly to thermal emission or additional neutrino emission. These subsequent interactions are largely model-dependent and will not be considered further here.

The equilibrium distribution N_p calculated as above is then used to determine the source functions of photons produced directly via proton synchrotron or via π^0 decay. The source functions of $e^{\pm}$ produced directly in $(p\gamma, e^{\pm})$ or indirectly via $\pi^{\pm}$ decays are calculated at the same time. These are necessary to get the source functions of photons emitted in the $e^{\pm}$-synchrotron process. Simultaneously, the source functions of the charged pions and muons are used in obtaining the source functions of photons originating in $(\pi^{\pm}\boldsymbol{B})$ and $(\mu^{\pm}\boldsymbol{B})$ processes. In the approximation where subsequent cascades can be neglected, the photon spectra are then obtained immediately from these source functions.

In Figure 3 we show the basic components of the photon energy spectrum produced as a result of the interaction of the relativistic protons with both the X-ray radiation field and the

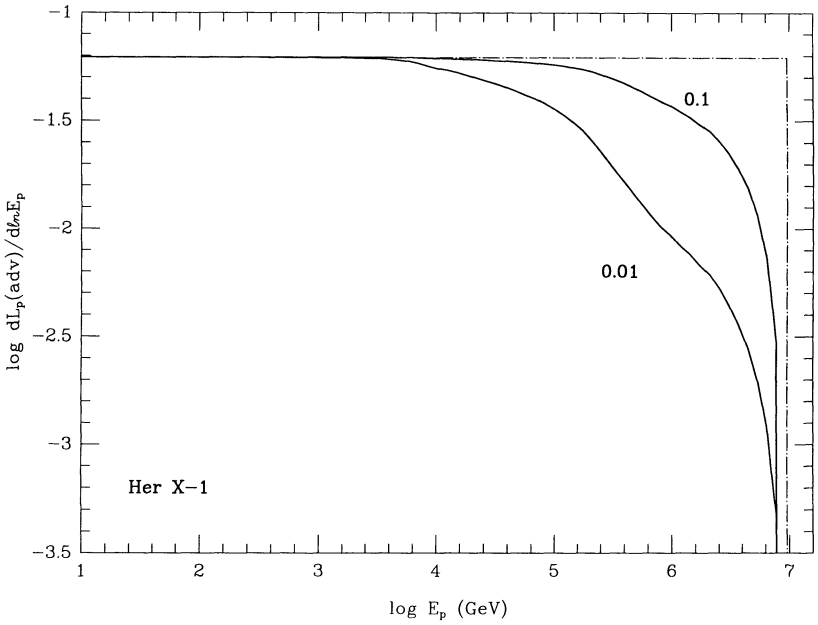

FIG. 2*a*

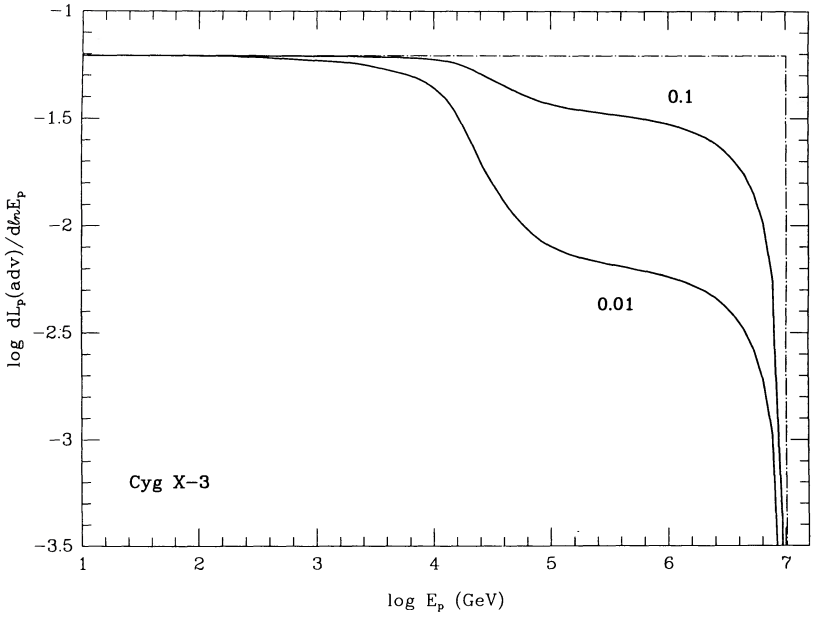

FIG. 2*b*

FIG. 2.—(*a*) Proton luminosity per logarithmic energy bandwidth (see eq. [6]), shown for the escaping protons after cooling losses, for the case of Her X-1. Curves are labeled with V_{adv}/c values. The luminosity is expressed in units of the total injected proton luminosity L_p(inj). The dash-dot line shows the initial proton distribution (see eq. [1]). (*b*) Same as (*a*), but for the case of Cyg X-3, using the canonical field $B_m = 10^6$ G.

canonical magnetic field values in the cases of Her X-1 and Cyg X-3. To illustrate the relative energetic importance of the different components, the spectrum is given in terms of photon luminosities per logarithmic energy bandwidth, normalized in units of L_p(inj). Each component of the spectrum is presented for two different values of V_{adv}/c, 0.1 and 0.01. In Figure 4 the total spectra are shown (all photon components added up), for Her X-1 with the magnetospheric field B_m derived from surface field observations, and for Cyg X-3 with five values of B_m, normalized in units of the injected proton luminosity L_p(inj), for $V_{adv}/c = 0.01$.

It is seen from Figures 3 and 4 that although in this type of diffusive shock the protons are unlikely to reach energies much above 10^7 GeV, this is sufficient to obtain a photon specturm extending into the PeV range. The dominant portion of the very high energy photons comes from the π^0 decays. Another contribution, which to the knowledge of the authors has not so far been pointed out in the literature, comes from synchrotron radiation of ultrarelativistic $e^{\pm}$ pairs from $\pi^{\pm}$ decays; this component competes at TeV energies with the π^0 component in low-B_m cases for Cyg X-3. The lower limit of the photon energy to which the π^0 component can extend depends on the location

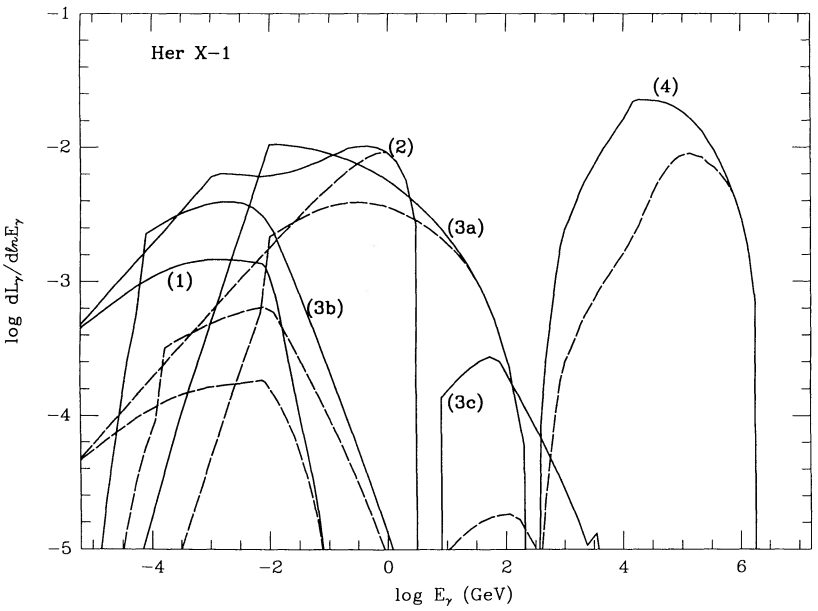

FIG. 3*a*

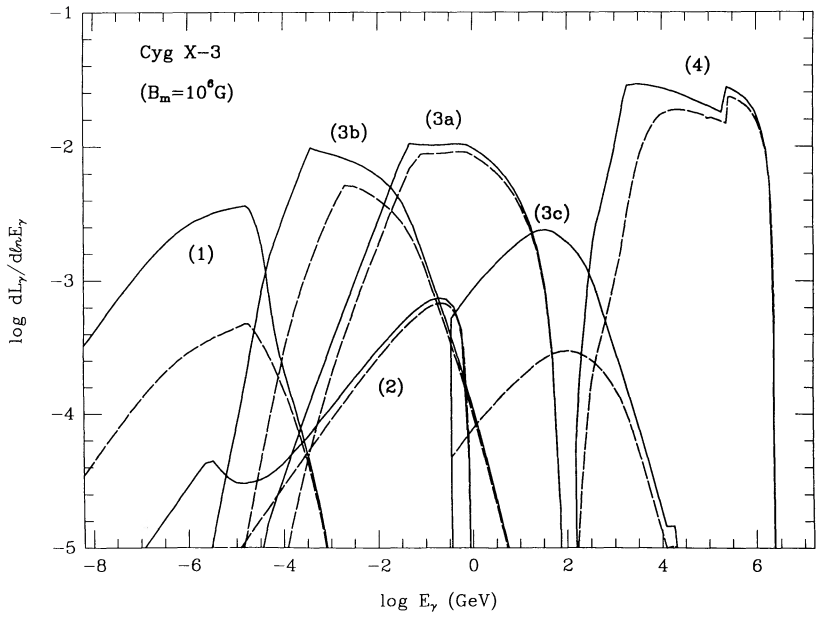

FIG. 3*b*

FIG. 3.—(*a*) Luminosity of photons per logarithmic energy bandwidth formed via ($p\gamma$) and ($p\boldsymbol{B}$) interactions, shown for the case of Her X-1. Continuous and dashed lines correspond to $V_{adv}/c = 0.01$ and 0.1, respectively. The spectrum consists of six components which are labeled with numbers: (1) photons emitted in the synchrotron process ($e^{\pm}\boldsymbol{B}$), where the $e^{\pm}$ pairs come from ($p\gamma$, $e^{\pm}$); (2) photons emitted in the proton synchrotron process ($p\boldsymbol{B}$); (3) photons emitted in the synchrotron process involving charged pions as well as subsequent products of their decay, i.e., muons and then electrons. This component therefore spilts into three subcomponents, which are ($\pi^{\pm}\boldsymbol{B}$((labeled 3a), ($\mu^{\pm}\boldsymbol{B}$) (labeled 3b), and ($e^{\pm}\boldsymbol{B}$) (labeled 3c). (4) photons coming directly from π^0 decay. Here, and in all subsequent figures, the luminosity in the *y*-axis is normalized in units of the total injected proton luminosity L_p(inj). (*b*) Same as (*a*), but for the case of Cyg X-3 with the "canonical" value of the magnetic field $B_m = 10^6$ G.

of the break in the hard X-ray spectrum of the source. Other spectral features in the X-ray spectrum are essentially unimportant here because at threshold $K_\pi^{\rm eff}$ stays always close to 0.14. This lower limit ($\propto K_\pi^{\rm eff}/E_{\rm break}$) is located around 100 GeV, for an X-ray break placed at a few tens of keV (typical for AXPs).

The low- and medium-energy gamma-ray flux (MeV–GeV) is produced partly by the contributions from proton synchrotron emission and synchrotron emission of $e^{\pm}$ pairs following from ($p\gamma$, $e^{\pm}$) reactions. The ($p\gamma$, $e^{\pm}$) component, because of the very low values of $K_e^{\rm eff}$ at $\gamma_p \rightarrow \gamma_{p,\,\rm max}$ (see also § 3), is always located well below 1 GeV (note that both these components do extend down to the X-ray range but cannot dominate the "primary" X-ray flux). However, the ($\pi^{\pm}\boldsymbol{B}$) and ($\mu^{\pm}\boldsymbol{B}$) synchro-

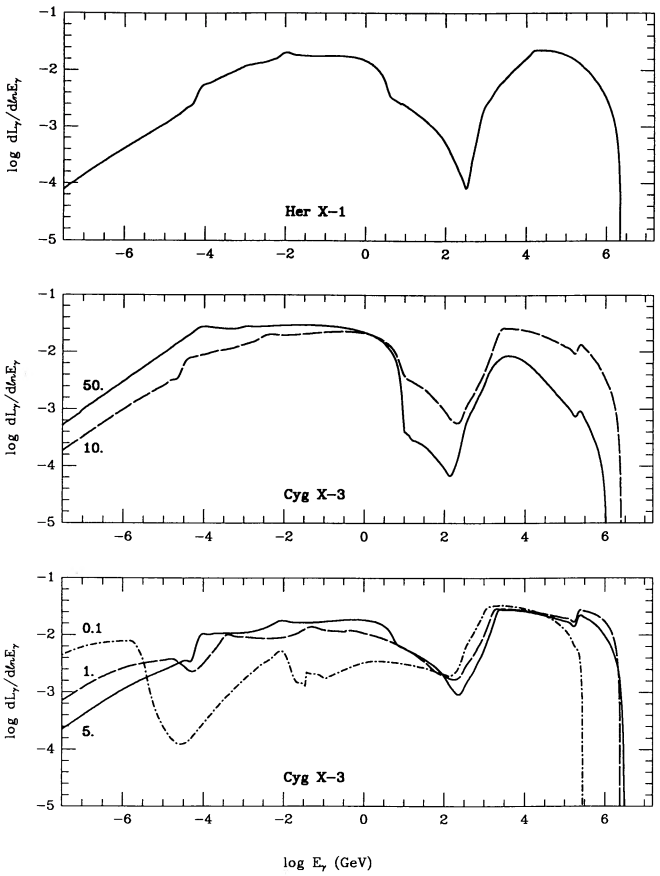

FIG. 4.—Total luminosity of photons in units of L_p(inj), shown for $v_{adv}/c = 0.01$. The upper panel is for Her X-1 (all components drawn with continuous lines on Fig. 3*a* are added). The middle and lower panels are for Cyg X-3, and curves are labeled with values of $B_m/10^6$ G. The sum of components which are drawn with the continuous lines on Fig. 3*b* (i.e., for a "canonical" value of B_m) is given by the long-dashed line in the lower panel.

tron components play an equal or even a major role in the MeV–GeV range, provided the magnetic field is not too high (see Fig. 3 and the bottom panel of Fig. 4).

We describe now the method used to calculate the synchrotron radiation from the charged pions and their charged decay particles (muons and $e^{\pm}$), as well as the resulting neutrino source functions. The synchrotron radiation from charged pion and their decay products (muons and electron/positron pairs) is obtained by first calculating N_p from equation (5). The source function of charged pions (the subscript π will refer to the $\pi^{\pm}$ quantities) is then obtained using the following approximation:

$$Q_\pi E_\pi dE_\pi = f_\pi N_p(E_p)\Lambda(p\gamma, \pi)E_p \, dE_p \,, \tag{7}$$

where $f_\pi = \frac{1}{2}$ (the other half of the energy goes into neutral pions). Charged pions are subject to decay [on a time scale $t_d(\pi) = \gamma_\pi \times 2.6 \times 10^{-8}$ s] and advection, as well as to synchrotron cooling. Therefore, the equation for N_π analogous to equation (5) yields

$$N_\pi = \begin{cases} \dfrac{1}{E_\pi \Lambda(\pi \boldsymbol{B})} \displaystyle\int_{E_\pi}^{E_{\pi,\max}} Q_\pi(z)\, dz & \text{for } \Lambda(\pi\boldsymbol{B}) > t_d^{-1}(\pi) + t_{\rm adv}^{-1}, \\ Q_\pi [t_d^{-1}(\pi) + t_{\rm adv}^{-1}]^{-1} & \text{elsewhere.} \end{cases} \tag{8}$$

With N_π at hand we can now calculate the source functions of (1) the $(\pi \boldsymbol{B})$ photons, denoted Q_γ, (2) muons, denoted Q_μ, and also (3) muon (anti)neutrinos, denoted $Q_\nu^{(1)}$:

$$Q_\gamma E_\gamma dE_\gamma = N_\pi \Lambda(\pi \boldsymbol{B}) E_\pi \, dE_\pi \,, \tag{9a}$$

$$Q_\mu E_\mu dE_\mu = f_\mu N_\pi t_d^{-1}(\pi) E_\pi \, dE_\pi \,, \tag{9b}$$

$$Q_\nu^{(1)} E_\nu^{(1)} dE_\nu^{(1)} = f_\nu^{(1)} N_\pi t_d^{-1}(\pi) E_\pi \, dE_\pi \,. \tag{9c}$$

Here $f_\mu + f_\nu^{(1)} = 1$ with $f_\mu = 3/4$. Also, $E_\mu/E_\pi = 3/4$, and we assumed $E_\nu^{(1)}/E_\pi = 1/4$. To follow the fate of the muons, we use Q_μ from equation (9b), and by analogy to pions, we obtain first N_μ and then the source functions of all the muon products, i.e., (1) $(\mu \boldsymbol{B})$ photons giving Q_γ, (2) electrons/positrons giving Q_e, and (3) electron/muon (anti)neutrinos giving $Q_\nu^{(2)}$:

$$Q_\gamma E_\gamma dE_\gamma = N_\mu \Lambda(\mu \boldsymbol{B}) E_\mu \, dE_\mu \,, \tag{10a}$$

$$Q_e E_e dE_e = f_e N_\mu t_d^{-1}(\mu) E_\mu \, dE_\mu \,, \tag{10b}$$

$$Q_\nu^{(2)} E_\nu^{(2)} dE_\nu^{(2)} = f_\nu^{(2)} N_\mu t_d^{-1}(\mu) E_\mu \, dE_\mu \,, \tag{10c}$$

where the subscript e refers to the $e^{\pm}$ quantities. Here $f_e + f_\nu^{(2)} = 1$ with $f_e = \frac{1}{3}$, and we assumed $E_e/E_\mu = \frac{1}{3}$, and $E_\nu^{(2)}/E_\mu = \frac{1}{3}$. The numerical values of $f_\mu, f_\nu^{(1)}, f_\nu^{(2)}, f_e$ were chosen in such a way that in the limiting case $t_d(\pi) \to 0$, $t_d(\mu) \to 0$ (or equivalently $B_m \to 0$) we reproduce the assumed equipartition of the total available charged pion energy between the three final neutrinos and the lepton: a fraction $f_\pi(f_\nu^{(1)} + f_\mu f_\nu^{(2)}) = \frac{3}{8}$ of proton energy lost by the proton in the $(p\gamma, \pi)$ process goes into neutrinos, and the rest, i.e., $f_\pi f_\mu f_e = \frac{1}{8}$ goes into electrons.

The ultrarelativistic $e^{\pm}$ pairs with the source function given by equation (10b) are subject to synchrotron cooling. To find the source function for these synchrotron photons, Q_γ, we make use of the following approximation:

$$Q_\gamma E_\gamma dE_\gamma = N_e(E_e)\Lambda(e^{\pm}\boldsymbol{B}) E_e \, dE_e \,. \tag{11}$$

The electron spectral density $N_e(E_e)$ can be obtained from a kinetic equation analogous to equation (5), with the advection term dropped [$\Lambda(e^{\pm}\boldsymbol{B}) \gg t_{\rm adv}^{-1}$],

$$\frac{\partial}{\partial E_e}(N_e \Lambda(e^{\pm}\boldsymbol{B}) E_e) = -Q_e \,, \tag{12}$$

where the electron source function Q_e satisfies equation (10b). Finally, one obtains

$$Q_\gamma = \frac{1}{E_\gamma}\frac{dE_e}{dE_\gamma}\int_{E_e}^{E_{e,\max}} Q_e(z) dz \,. \tag{13}$$

We comment now on some of the discontinuities or jumps that appear in the π^0 and $(e^{\pm}\boldsymbol{B})$ spectral components, e.g., in Figure 3*b*. The sharpness of these features is of course artificial, being introduced by our piecewise analytical approximations. The jump in the π^0 component (the highest energy component) in Cyg X-3 around $10^{5.5}$ GeV is due entirely to the fact that the inelasticity $K_\pi^{\rm eff}$ computed for the X-ray spectrum of Cyg X-3 has already reached a plateau of 0.5 at $\gamma_p = 10^6$, i.e., well before $\gamma_{p,\max}^{\rm Cyg\ X\text{-}3} = 10^7$. This feature is not visible in the π^0 component of Her X-1 (Fig. 3*a*) because the different X-ray spectrum gives a different behavior of $K_\pi^{\rm eff}$ versus γ_p. In Her X-1, $K_\pi^{\rm eff}$ increases monotonically with γ_p and reaches a value of 0.5 only at $\gamma_p \approx \gamma_{p,\max}^{\rm Her\ X\text{-}1} = 10^7$. The small jump around 10^4 GeV in the $(e^{\pm}\boldsymbol{B})$ component (the second component from the right in Fig. 3) comes, however, from effects associated with the quantum regime of the synchrotron radiation. The $e^{\pm}$ pairs (eq. [10b]) reach sufficiently high energies that in the presence of a mag-

netic field $B_m \sim 10^6$ G the classical formula for the typical energy of a photon emitted via $(e^{\pm}\boldsymbol{B})$ is no longer valid, since E_γ cannot exceed the kinetic energy of the parent particle (e.g., Pavlov & Golenetskii 1986). We therefore took

$$E_\gamma = \min\left(\frac{4}{3}\frac{E_e^2}{m_e c^2}\frac{B_m}{B_{\mathrm{cr},e}}, E_e\right) \quad (14)$$

in equation (11), where $B_{\mathrm{cr},e} = m_e^2 c^3/e\hbar = 4.413 \times 10^{13}$ G. This approximation ensures a smooth transition from the classical expression for the synchrotron cooling rate (eq. [3a] with the term m_e/m_X dropped) to its quantum counterpart given by Brainerd & Petrosian (1987) (their eqs. [1]–[4]), which at $E_\gamma \approx E_e$ gives

$$\Lambda(e^{\pm}\boldsymbol{B}) = 1.79 \times 10^9 \gamma_e^{-1/3} B_m^{2/3} . \quad (15)$$

Reaching the quantum regime in the synchrotron emission can lead to a steepening of the classical photon spectrum (Brainerd & Petrosian 1987), but only in those situations where the electron density $N_e(E_e)$ is being maintained at the same prescribed value (i.e., by external means). In our case, however, the electron distribution is controlled by the losses, so that the change in the photon spectrum when the quantum regime is reached around 1.7×10^4 $(B_m/10^6\ \mathrm{G})^{-1}$ GeV (which because of the approximations looks like a jump) occurs in the opposite direction: $N_e(E_e)$ flattens because the rate $\Lambda(e^{\pm}\boldsymbol{B})$ entering equation (12) drops in the quantum regime. Other changes of slope in the spectra are caused by the onset of the effect of cooling losses on the particle distribution. The very sharp drops at the low- and high-energy ends of the various spectral components are of course merely a result of the simplified steplike cutoffs in the input proton distribution.

Another product of the reactions described above is neutrinos. The source functions for high-energy neutrinos appeared in equations (9c) and (10c) when the photon components due to $(\pi^{\pm}\boldsymbol{B})$, $(\mu\boldsymbol{B})$, and $(e^{\pm}\boldsymbol{B})$ were assessed. The expected neutrino spectra for Her X-1 and Cyg X-3 are shown in Figure 5, with the luminosity normalized to the proton luminosity L_p(inj). The neutrinos are energetic enough to be potentially capable of affecting the internal structure and evolution of secondary companions in both systems. The consequences of neutrinos arising in proton beam dumping on the surface of the secondary companion of Cyg X-3, e.g., as calculated by Gaisser et al. (1986), are expected to be dramatic.

6. RESULTS AND CONCLUSIONS

We have calculated the high-energy proton spectra as well as the photon and neutrino spectra which are expected to form in the magnetospheres of accreting pulsars, in the presence of the interactions between the relativistic protons and the accreting pulsar X-ray radiation field as well as the magnetospheric field. Some of the simplifications employed in the calculation are worth mentioning. The optically thin approximation, which is entirely appropriate for neutrinos, is a rough approximation for photons. The latter may be involved in $\gamma\gamma$ absorptions initiating pair cascades. Another approximation consists of ignoring additional possible effects on the photon spectrum after the photons leave the site of their formation, e.g., involving absorption by far-infrared photons coming from another source (companion star, disk). We have also neglected any beaming effects, which are much more model-dependent, and have restricted ourselves to a calculation of angle-averaged fluxes. These restrictions can be lifted in a more detailed analysis, which is currently underway. The above approximations appear reasonable for a simple first-order model as intended here, which is designed to provide useful insights concerning the type of spectra and the relative strengths of the various components that are involved.

Our calculations can be used to investigate the constraints on the radiation density of X-rays, magnetic field strength, and acceleration mechanisms necessary to photons with energies of 10^{15} eV or higher as reported. Even though there are many parameters that can be varied (V_{shock} and the radiation density

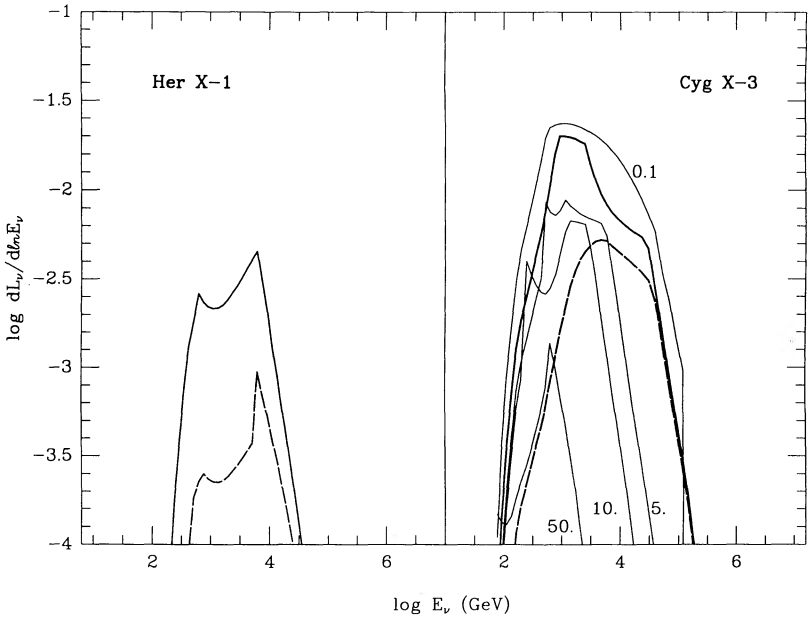

FIG. 5.—Neutrino luminosity per logarithmic energy bandwidth formed via $\pi^{\pm}$ and $\mu^{\pm}$ decays, normalized to L_p(inj), for the case of Her X-1 (*left*) and Cyg X-3 (*right*). Continuous and dashed lines correspond to $V_{\mathrm{adv}}/c = 0.01$ and 0.1, respectively. For Cyg X-3, the case of the canonical value of B_m is emphasized with thick lines. For other values of B_m curves are thin and are labeled with the value of $(B_m/10^6\ \mathrm{G})$.

u_X among them), there are some obvious physical constraints that limit the highest possible $\gamma_{p,\max}$. In particular, relativistic shocks with $V_{\rm shock}/c$ very close to unity (which are potentially promising, since they appear more efficient than classical shocks; e.g., Ellison, Jones, & Reynolds 1990) are probably difficult to achieve in the case of stellar objects; also, a low value of the density of the X-ray radiation field would allow synchrotron cooling to take over, thus diminishing the total luminosity of photons in the TeV–PeV range. Adding the restrictions coming from the proton confinement argument, it is evident that there is not much room for significant variations in either B_m or u_X; to observe anything like the claimed fluxes of VHE/UHE gamma rays, these parameters should not differ too much from the nominal values used here. However, these nominal values are essentially the standard observational values for bright AXPs, among which are the objects with reported VHE/UHE detections.

It is worth emphasizing that the calculations presented depend on the choice of the input proton spectrum (or the particular proton acceleration model) in two ways. First, different acceleration rates can give different values of $\gamma_{p,\max}$, which fixes the locations of the high-energy cutoffs for all the components in the electromagnetic spectrum. As a result of the general considerations above and in § 3, we do not expect proton energies to exceed 10^7 GeV for standard diffusive shock acceleration in neutron star environments. Somewhat higher energies, however, may be attained under oblique shock conditions, where the acceleration time can be shorter than for parallel diffusive shocks assumed here by a factor of 10–30 (e.g., Drury 1983; Jokipii 1987; Takahara & Terasawa 1990), leading to larger proton, photon, and neutrino energies by a factor roughly proportional to $t_{\rm acc}^{1/2}$. A maximum upper limit on the Lorentz factor $\gamma_{p,\max}$ would then be imposed by the confinement requirement, $\gamma_p \lesssim \gamma_{p,\rm conf}$, marked with thin long-dashed lines in Figures 1*a* and 1*b*. A second way in which the calculations depend on the input proton spectrum is through the power-law index assumed, which for different acceleration mechanisms may differ from the -2 input index assumed in equation (1). This is an important factor in fixing the relative energetic contributions of the MeV–GeV and the TeV–PeV portions of the secondary spectrum.

The calculated photon spectra consist of six distinct components covering a wide range of photon energies. These are due, respectively, to the following effects: π^0 decay; $(\pi^{\pm}\boldsymbol{B})$, $(\mu^{\pm}\boldsymbol{B})$, and $(e^{\pm}\boldsymbol{B})$ following $\pi^{\pm}$ creation; $(p\boldsymbol{B})$; and $(e^{\pm}\boldsymbol{B})$ following $(p\gamma, e^{\pm})$, which appear in Figure 3. The detailed structure of each component and their relative importance depends on the density of the X-ray–UV radiation field, its spectral composition, and the strength of the magnetic field involved. However, some general features or properties which are largely model-independent may be predicted without going into a detailed analysis. We describe these briefly below.

First of all, it is straightforward to infer the value of Γ_p, the slope of the relativistic proton source function, by looking at the $(p\boldsymbol{B})$ component. Even without accurate calculations of the synchrotron radiation spectrum (involving a convolution procedure), our simplified approach is exact enough to yield the proper solution, e.g. for a power-law distribution of proton densities $N_p \propto E_p^{-\delta}$ the resulting photon power spectrum $E_\gamma(dL_\gamma/dE)$ $(\equiv dL_\gamma/d\ln E_\gamma)$ goes as

$$E_\gamma(dL_\gamma/dE) \propto E_\gamma^{-(\delta-3)/2}, \tag{16}$$

where dL_γ/dE is the energy spectrum. In this energy region of N_p where the advection rate exceeds the total cooling rate (the low-E_p range; see also Fig. 2), we have $\delta = \Gamma_p$. Thus, in our case $\delta = 2$ and $E_\gamma(dL_\gamma/dE) \propto E_\gamma^{0.5}$, which is the behavior seen in Figures 3 and 4. The approximate shape of that component at higher energies, where the total cooling rate becomes greater than the advection rate, may also be guessed, once we are sure that $(p\boldsymbol{B})$ is more important than the $(p\gamma)$ cooling (e.g., the case of Her X-1, or the cases of Cyg X-3 with $B_m > 10^6$ G). Making use of equations (3a) and (5), we obtain $N_p \propto E_p^{-(\Gamma_p+1)}$, and for $\Gamma_p = 2$ we get $E_\gamma(dL_\gamma/dE) \propto E_\gamma^0$. This roughly reproduces the exact shape shown for Her X-1, and is in excellent agreement with the more exact results for Cyg X-3 with $B_m = 5 \times 10^7$ G (see the middle panel of Fig. 4). In the latter case, virtually all of the spectrum up to the break at ~ 10 GeV is due to $(p\boldsymbol{B})$ alone. The π^0 component aside, the only other component which matters in this case is due to $(\pi^{\pm}\boldsymbol{B})$ building up the bottom of the dip centered at -50 GeV.

Another interesting feature which is expected in the MeV spectral range and below is the synchrotron contribution of pairs from the $(p\gamma, e^{\pm})$ process. Since this component cannot extend as far in photon energies as the $(p\boldsymbol{B})$ component, it produces a clearly distinguishable feature superposed on the $(p\boldsymbol{B})$, provided that the UV/X-ray radiation energy density μ_X exceeds the magnetic energy density u_B for the particular value of B_m. [Note that according to Fig. 1*a*, a decreasing value of B_m increases the importance of $(p\gamma, e^{\pm})$ relative to both $(p\boldsymbol{B})$ and $(p\gamma, \pi)$. This is the case for Cyg X-3 with $B_m = 10^5$ G shown in Figure 4 (*bottom panel*). This case is particularly interesting also because as the $(p\boldsymbol{B})$ contribution becomes negligible, the two more exotic components $(\mu^{\pm}\boldsymbol{B})$ and $(e^{\pm}\boldsymbol{B})$ dominate the MeV–GeV range, peaking at ~ 10 MeV and at ~ 3 GeV, respectively.] Therefore, whatever the value of B_m is, we expect a substantial change in the spectral slope to occur at photon energies below 1 MeV. This may be detectable with instruments like the OSSE or COMPTEL detectors on the *GRO* spacecraft.

The *GRO* EGRET detector, which reaches energies as high as 30 GeV, provides also a unique opportunity to look at another interesting part of the spectrum, which is the transition between the "regular" gamma-ray part of the spectrum, i.e., the part below ~ 10 GeV due in most cases to the $(p\boldsymbol{B})$ component, and the low-energy part of the π^0 component. The transition region, which consists either of the $(\pi^{\pm}\boldsymbol{B})$ component (high-B_m) or the $(e^{\pm}\boldsymbol{B})$ component (low-B_m), has the shape of an asymmetrical dip almost two decades in energy wide, centered around ~ 50 GeV and attaining a minimum slightly above 100 GeV.

The neutrino luminosity plotted in Figure 5 includes both muon and electron neutrinos. The muon neutrinos, upon reaching Earth, can induce a muon signal in an appropriate underground or undersea muon detector. To estimate the muon flux, we need to specify a value for L_p(inj), which is the scaling factor in Figure 5, as well as the distance to the source D. Taking a value $L_p(\text{inj}) = 10^{39}$ ergs s^{-1}, $D = 10$ kpc, and the canonical value $B_m = 10^6$ G for Cyg X-3 as an example, we can calculate the neutrino flux dN_ν/dE_ν. The muon signal is estimated using the probability for neutrino to muon conversion in a detector given by Gaisser & Stanev (1985b), with a low-energy cutoff for muons equal to $E_\mu = 100$ GeV. The resulting number of events for Cyg X-3 is 1.5×10^{-15} cm^{-2} s^{-1} for $V_{\rm adv}/c = 0.01$, and 7.7×10^{-16} for $V_{\rm adv}/c = 0.1$. These muon signals are slightly lower than those listed by Gaisser & Stanev (1985a) and Kolb, Turner, & Walker (1985) for a pp beam-

dump model. Whereas in their case the results depend somewhat on the density of target material where the neutrinos are produced, in our case the neutrinos come from $p\gamma$ interactions and the results depend on the assumed source X-ray spectrum and magnetic energy density. As seen from Figure 5, the neutrino signal increases as the magnetic field B_m is lowered, since less energy goes into other (photon) channels. For underground detectors, the upward-directed muon signal would be below typical observational upper limits for existing facilities of this type (e.g., Svoboda et al. 1987; Oyama et al. 1989) which are of the order of a few $\times 10^{-14}$ cm^{-2} s^{-1} or less. However, with the source parameters as above, the muon signal predicted by this model is on the margin of detectability by DUMAND. If the angular resolution of the DUMAND Octagon array is 1° (Stenger 1990), the signal from the neutrino flux of Cyg X-3 would dominate that from the neutrino flux of atmospheric origin (Fig. 7 in Stanev 1990), already above $E_\nu \sim$ 100 GeV. In the case of Her X-1 the distance is about 6 kpc, so the neutrino flux as a ratio of L_p(inj) would be comparable, but the observational estimates of L_p(inj) are typically lower than for Cyg X-3. Taking for Her X-1 the value $L_p(\mathrm{inj}) = 10^{38}$ ergs s^{-1} and $D = 6$ kpc, the muon signal above 10^2 GeV is 0.9×10^{-16} and 1.6×10^{-17} cm^{-2} s^{-1} for $V_{\mathrm{adv}}/c = 0.01$ and 0.1, respectively, somewhat below the nominal DUMAND observability limit. Note that for simplicity this signal was calculated assuming an isotropic pattern of neutrino emission. If the angular distribution of ultrarelativistic protons is confined to a cone with an opening angle 2α, the generated neutrinos will presumably follow this distribution too. If the cone crosses the observer's line of sight during its rotation, the rotationally averaged flux will be higher than the isotropic flux [assuming an identical L_p(inj) in both cases] by a factor $2\alpha/[\pi(1 - \cos\alpha)]$. Thus, for a moderate opening angle $2\alpha \sim 20°$, there would be an additional amplification factor of ~ 10.

The efficiency of conversion of the proton luminosity into photons or neutrinos, $L_{\gamma,\nu}(\mathrm{tot})/L_p(\mathrm{inj})$, is for our range of parameters most sensitive to the advection rate, and for the latter species also to the magnetic field value. A radial accretion flow in the vicinity of the magnetosphere leads to a smaller ratio of the high-energy photon (neutrino) luminosity to the injected proton luminosity than is obtained in the case of a disk accretion flow. The absolute value of the total luminosity L_p(inj) is essentially a free parameter in all theoretical models discussed in the literature, including this one. This is because the efficiency of acceleration is theoretically uncertain, and the character of the accretion flow near the magnetosphere determining the advection rate is poorly known. Similarly, the observational status of the absolute level of the claimed TeV–PeV flux observed from AXPs is highly uncertain, because of questions of poorly determined duty cycles and incomplete time coverage, as well as serious doubts about statistics. For these reasons, two of the main purposes of our calculation here have been (1) to provide detailed theoretical spectra extending over a wide range of energies, to compare with observations and provide some handle on the relative strengths of various components, and (2) to offer a possible method to resolve the uncertainty about the absolute flux level in the TeV/PeV range by making use of the MeV/GeV components, which may be more reliably observed and analyzed. This opens the possibility for a determination of L_p(inj) with *GRO*–type observations, which may then be confronted with the observations in the TeV–PeV range.

This research has been supported in part through grants NASA NAGW-1522, NSF AST 8815266, and (P. M.) the CfA Smithsonian Visiting Scientist program. We are grateful to I. Axford, A.M. Hillas, B. Paczyński, and M. Sikora for useful comments and discussions, and to W. Kluźniak for critical remarks on the manuscript.

REFERENCES

Axford, W. I. 1981, Proc. 17th Internat. Cosmic Ray Conf. (Paris), 12, 155
Begelman, M. C., Rudak, B., & Sikora, M. 1990, ApJ, 362, 38 (BRS)
Bonnet-Bidaud, J.-M., & Chardin, G. 1988, Phys. Rept., 170, (No. 6), 325
Brainerd, J. J., & Petrosian, V. 1987, ApJ, 320, 703
Drury, L. O'C. 1983, Rept. Progr. Phys., 46, 973
Ellison, D. C., Jones, F. C., & Reynolds, S. P. 1990, ApJ, 360, 702
Fegan, D. J. 1990, Proc. 21st Internat. Cosmic Ray Conf. (Adelaide), 2
Gaisser, T. K., & Stanev, T. 1985a, Phys. Rev. Letters, 54, 2265
———. 1985b, Phys. Rev. D, 30, 985
Gaisser, T. K., Stecker, F. W., Harding, A. K., & Barnard, J. J. 1986, ApJ, 309, 674
Jokipii, J. R. 1987, ApJ, 313, 842
Kazanas, D., & Ellison, D. C. 1986, ApJ, 304, 178
Király, P., & Mészáros, P. 1988, ApJ, 333, 719 (KM)
Kolb, E. W., Turner, M. S., & Walker, T. P. 1985, Phys. Rev. D, 32, 1145
Lang, K. R. 1980, Astrophysical Formulae (Berlin: Springer-Verlag), 453
McCray, R. A., Shull, J. M., Boynton, P. E., Deeter, J. E., Holt, S. S., White, N. E. 1982, ApJ, 262, 301
Mihara, T., et al. 1990, Nature, 346, 250
Mitra, A. 1990, A&A, 234, L5
Orth, C. D., & Buffington, A. 1976, ApJ, 206, 312
Oyama, Y., et al. 1989, Phys. Rev. D, 39, 1481
Pavlov, G. G., & Golenetskii, S. V. 1986, Ap&SS, 73, 33
Stanev, T. 1990, Nucl. Phys. B. (Proc. Suppl.), 14A, 17
Stenger, V. J. 1990, Nucl. Phys. B. (Proc. Suppl.), 14A, 153
Svoboda, R. C., et al. 1987, ApJ, 315, 420
Takahara, F., & Terasawa, T. 1990, in Astrophysical Aspects of the Most Energetic Cosmic Rays, ed. M. Nagano (Tokyo: Tokyo Univ.), in press
Weekes, T. C. 1988, Phys. Rept., 160, 1
———. 1990, in Proc. Snowmass High Energy Physics Meeting, in press
White, N. E., & Holt, S. S. 1982, ApJ, 257, 318